

# Quantitative characterization of lamellar microstructure of plasma-sprayed ceramic coatings through visualization of void distribution

Chang-Jiu Li\*, Wei-Ze Wang

*State Key Laboratory for Mechanical Behavior of Materials, School of Materials Science and Engineering,  
Xi'an Jiaotong University, Xi'an, Shaanxi 710049, PR China*

Received 1 April 2004; received in revised form 21 June 2004

## Abstract

The visualization of the detailed microstructure of plasma-sprayed ceramic coating was realized through energy dispersed X-rays (EDX) line analysis of the distribution of an infiltrated element as a tracer. A method was proposed based on an idealized lamellar structure model that the coating consisted of a stacking of lamellae with an identical thickness and the EDX line distribution of a tracer in the coating to quantitatively characterize the microstructure of plasma-sprayed coatings. The characterization was performed using structural parameters including lamellar bonding ratio, mean lamellae thickness and interlamellar gap size distribution. The experiment was carried out using plasma-sprayed alumina coating with the infiltration of  $\text{Cr}_2\text{O}_3$  as the tracer through chromic acid. The measurement yielded a mean bonding ratio of 32% between the lamellar interfaces, a mean lamellae thickness of  $1.2\text{ }\mu\text{m}$  and a bimodal distribution for interlamellar gaps. The mean bonding ratio was defined as the ratio of the total bonded area to the total apparent interface area. These results agreed well with previously reported results obtained by copper plating technique. It was revealed that the proposed method could be applied to quantitatively characterize the lamellar structure of plasma-sprayed coatings.

© 2004 Elsevier B.V. All rights reserved.

**Keywords:** Plasma spraying; Ceramics; Coatings; Microstructure; Quantitative characterization

## 1. Introduction

A thermally sprayed coating is formed by a stream of molten or softened droplets impacting on a substrate followed by flattening, rapid cooling and solidification processes. The individual molten droplets spread to form thin lamellae. The stacking of those lamellae constitutes the coating. Therefore, a thermally sprayed coating is generally of a lamellar structure. A fraction of porosity from several percent up to 20% can be formed in coatings [1] resulting from the insufficient filling and incomplete wetting of molten liquid on previously formed rough coating surfaces. Microcracks can be easily formed within the splats of brittle materials [2], in particular, ceramic materials owing to the quenching stresses that occur in splats [3], which also contribute to the total porosity.

Therefore, porosity has often been used as a microstructural parameter for thermal spray coatings.

Generally, the porosity in thermal spray deposits is characterized qualitatively by microstructural observation and quantitatively by the Archimedes's technique and mercury intrusion porosimetry (MIP) technique. Using the Archimedes's porosimetry measurement, only the total non-interconnected porosity can be obtained. The MIP measurement can evaluate quantitatively not only the total porosity for open voids but also the distribution of void size. The MIP measurement indicated that the voids in thermal spray deposits appeared as a bimodal distribution [4]. However, Kuroda's study suggested that the surface roughness may make MIP results misleading [5]. This results from the interconnection of large voids of a micrometer size through small voids of a sub-micrometer size. On the other hand, the recent study has clearly revealed that the properties of a thermal spray coating are dominated by the lamellar structure rather than the

\* Corresponding author. Tel.: +86 29 82660970; fax: +86 29 83237910.  
E-mail address: licj@mail.xjtu.edu.cn (C.-J. Li).

total porosity in the coating [6]. This is because most voids in the coating are of two dimensions feature and the sizes in two directions are much larger than the other one direction owing to the lamellar structure [2]. The non-bonded interface area exists at the interface between lamellae as voids [2,7] and plays a dominant part in determining the properties of the coating [6]. Accordingly, as far as a thermal spray coating is involved, the adhesion and cohesion of a thermal spray coating should be taken into account, which are concerned with the existence of the non-bonded interface area.

Recently, small angle neutron scattering (SANS) was also used to characterize the specific void surface area of ceramic deposits with the information about anisotropic features of the voids [8]. However, an examination of the relationship between the specific void surface area and mechanical properties of the deposit (for example wear resistance [9]) yielded a very poor dependence. Therefore, it is necessary to select other parameters to characterize the voids and the lamellar structure. Moreover, it is still difficult to quantitatively characterize the microstructure of sprayed coatings only through the direct use of optical microscopy and scanning electron microscopy (SEM) [2,10].

Previous studies [2,11,12] have visualized the lamellar structure of alumina coatings through the distribution of copper deposited into the voids in the coatings by electroplating. The distribution of copper on a cross-section of the copper-electroplated coating clearly revealed the existence of microvoids besides conventional coarse pores. Those microvoids can be divided into two categories: interlamellar voids and microcrack type voids. The interlamellar voids were observed as the non-bonded interface areas between flattened lamellae and the microcrack type voids as vertical cracks in individual flattened lamellae. It becomes possible to define a lamella in a coating and to examine detailed structures of the coating based on the distribution of the copper plated into the coating. Accordingly, the quantitative characterization of the microstructure using lamellar structural parameters rather than porosity becomes possible. Based on the tentative structure/properties relationships and the quantitative structural parameters, an estimation of coating properties becomes feasible. However, the limitation of the copper electroplating method was that this approach was not applicable to electrically conductive coatings including metallic, cermet and even some oxide ceramic coatings.

Therefore, some other approaches to infiltrate materials different from the coating elements have been attempted [13–16]. Most of those attempts were limited to the illustration of lamellar structure features and characterization of voids. This may be due to lack of proper quantitative characterization method for lamellar structures. On the other hand, those studies have illustrated that through using proper materials in a liquid state the materials, one of whose elements is completely different from all elements contained in the coatings, can be well infiltrated into voids including the lamellar interfaces in a plasma-sprayed coating.

In the present study, the visualization of the detailed microstructure of plasma-sprayed coatings was attempted through energy dispersed X-rays (EDX) line analysis of infiltrated material used as a tracer. A method to quantitatively characterize the microstructure of sprayed coatings was proposed through the processing of digital analysis of the infiltrated element.

## 2. Model for the evolution of the microstructural parameters based on the distribution of a tracer

### 2.1. The idealized model for the microstructure of thermally sprayed coatings

Through an examination of the microstructure of plasma-sprayed coatings using transmission electron microscopy (TEM), McPherson and Shafer underlined the existence of interlamellar voids between lamellae [7]. Previous studies have visualized lamellar structure features of plasma-sprayed alumina coatings and the existence of such voids between lamellae by the distribution of copper electroplated into plasma-sprayed alumina coatings [2,11,12]. Based on those results, an idealized lamellar structure for thermally sprayed coatings was proposed, as shown in Fig. 1. It can be assumed that the coating consists of a stacking of lamellae with an identical thickness of  $\delta$ . The whole lamellar interfaces are divided into the bonded interfaces and the non-bonded interfaces corresponding to lamellar voids. Those lamellar voids are of semi-two-dimensional features. The dimension in the direction perpendicular to the lamella, i.e., width of the non-bonded interface, is generally less than  $1\text{ }\mu\text{m}$ , while the dimensions at the directions along the lamella are comparable to the size of individual splat [2,6]. The width of the non-bonded interface area is defined to be  $\beta_i$ , and the lamellar

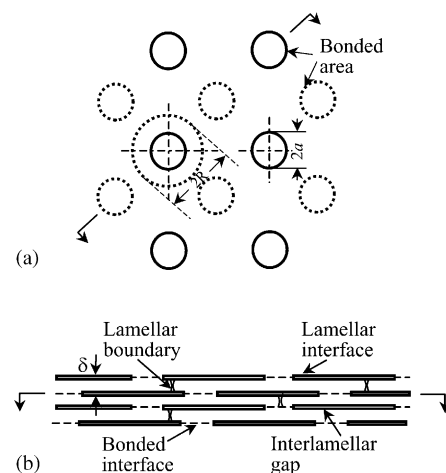


Fig. 1. Idealized model for the microstructure of thermally sprayed coating: (a) view parallel to the lamellar plane; and (b) view perpendicular to the lamellar plane.

bonding ratio  $\alpha$ . The bonded interface is distributed between lamellar interfaces in a form of circular area. The size of the bonded circular region is of a radius  $a$ . Each lamella may contain a network of vertical microcracks perpendicular to the lamellae. These vertical cracks occur in the coating of brittle materials, such as ceramics. For coatings sprayed with ductile metal, vertical cracks can be neglected. For a practical thermal spray coating, the tortuosity of a lamella may be considered as an additional parameter of coating structure.

## 2.2. Visualization of detailed lamellar structure of thermal spray coating

Because of submicrometer size features of lamellar voids in a thermal spray coating, it is generally impossible to identify those areas from a cross-sectional microstructure of the coating by conventional microstructural characterization approaches. Through the infiltration of materials into voids in the coating as a tracer, the direct visualization resulting from the distribution of the infiltrated materials on the cross-sectional microstructure is actually difficult owing to the limited contrast of infiltrated material and coating material when the characterization is performed using conventional optical or electron microscopes. In our study, the infiltration to the coating is first performed and then the tracer element contained in the infiltrated material is analyzed along lines perpendicular to lamella through a cross-section of the coating. In this way, the voids in the coating, and subsequently the lamellar structure can be visualized.

Fig. 2 shows a typical microstructure of plasma-sprayed alumina coating infiltrated by chromic oxide and a typical distribution of Cr along the marked line. The detailed plasma spray conditions and EDX analyzing conditions are given in the following Section 4. The voids filled with  $\text{Cr}_2\text{O}_3$  ap-

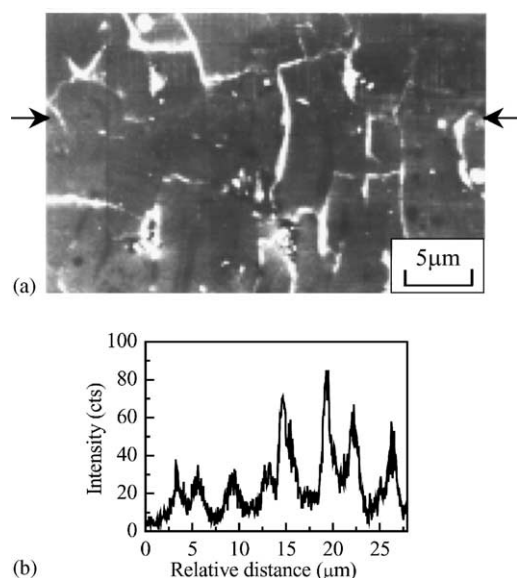


Fig. 2. (a) Typical microstructure of  $\text{Cr}_2\text{O}_3$  infiltrated  $\text{Al}_2\text{O}_3$  coating; and (b) Cr distribution along the line marked by arrows.

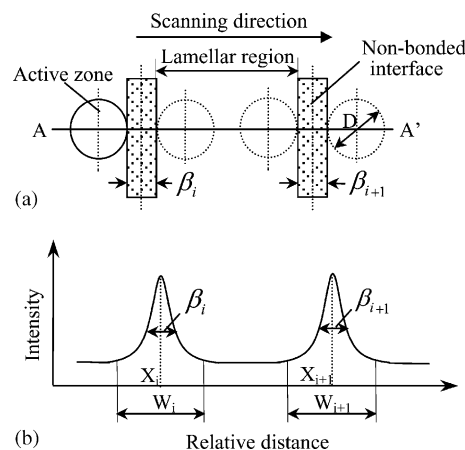


Fig. 3. Schematic of the evolution of the EDX peak of the tracer in a non-bonded interface.

peared white and the alumina matrix appeared gray within the microstructure. The peaks of the line analysis represent the distribution of chromium in infiltrated chromia and correspond to locations and states of lamellar voids. The distribution of chromium on the microstructure depicts the detailed distribution of voids in the coating.

## 2.3. Model for the evolution of the structural parameters from the tracer distribution in the coating

As for the idealized microstructure shown in Fig. 1, when all non-bonded interfaces between flattened particles can be filled up by the tracer sufficiently to be detectable by the EDX line analysis, the evolution of the EDX peak of the tracer is shown schematically in Fig. 3. Supposing that the effective reactive zone of the electron beam during the EDX analysis has a circular geometry when the periphery of the active zone of the electron beam comes into contact with the lamellar voids filled with the tracer, the EDX signal of the tracer begins to appear. With the movement of the active zone forward, the signal intensity increases. After the maximum intensity is achieved when the center of the active zone reached the middle of the non-bonded interface void, the signal intensity turns to decrease with the further movement of the active zone. When the active zone crosses over the void completely, the signal of the tracer becomes zero. As a result, a pulse signal for the tracer, as shown in Fig. 3(b) can be detected. For such a signal, the basic parameters include the abscissa of the center of the  $i$ th peak ( $X_i$ ) and the width of the  $i$ th peak ( $W_i$ ). The  $X_i$  in Fig. 3(b) corresponds to the middle position of the non-bonded interface. In this case, the lamellar thickness is equal to the interval between two adjacent non-bonded interfaces as shown by the following equation

$$\delta_i = X_{i+1} - X_i - \frac{\beta_i}{2} - \frac{\beta_{i+1}}{2} \quad (1)$$

where  $\delta_i$  is the lamellar thickness ( $\mu\text{m}$ ),  $\beta_i$  width of the  $i$ th lamellar interface void ( $\mu\text{m}$ ),  $\beta_i = W_i - D$  ( $D$  is diameter of the active zone,  $\mu\text{m}$ ).

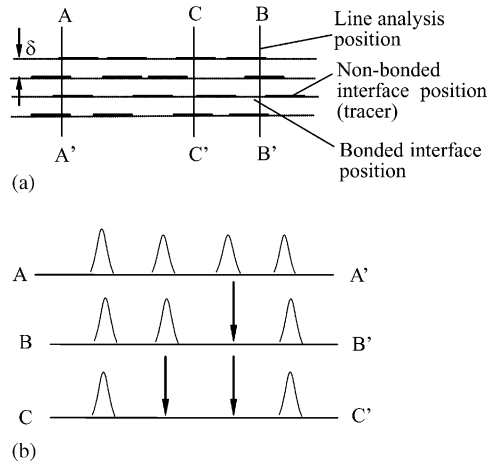


Fig. 4. (a) Schematic of the presence of distributions of the tracer corresponding to the non-bonded interface; and (b) typical three patterns for the peak presence of the tracer along EDX analysis lines marked. Arrows in (b) indicate the bonded interface position.

The cross-sectional microstructure of the coating with voids filled by the tracer is shown in Fig. 4(a). The distribution of the tracer corresponded to the non-bonded interface voids. When the EDX analysis along the line perpendicular to lamellae was carried out, as shown schematically by typical A–A', B–B' and C–C' lines, the peaks of the tracer appeared at the non-bonded interface void areas. The following three typical cases are illustrated in Fig. 4(b).

Case-I: no bonding between three adjacent lamellae. Four peaks of the tracer were detected one by one at the interfaces with the same peak spacing, as shown schematically by the distribution along A–A' line in Fig. 4(b).

Case-II: one bonded interface between two non-bonded interfaces, as shown by line B–B'. No tracer was present at the bonded interface and consequently no peak of the tracer appeared between the two adjacent non-bonded interfaces. Therefore, the spacing between the two adjacent peaks across bonded interface will be double the lamellar thickness.

Case-III: two adjacent interfaces bonded together. There was one non-bonded interface just at each side of those two bonded interfaces. The peaks of the tracer representing two non-bonded interfaces appeared at a large spacing equal to three times of lamellar thickness, as shown by C–C' in Fig. 4(b).

As a result, the number of the bonded interfaces between two adjacent non-bonded interfaces was equal to the ratio of peak spacing to lamellar thickness minus one for the idealized lamellar structure of identical lamellae thickness. Theoretically, the distribution of the frequency of the peak spacing presents characteristic peaks at integer times of the lamellar thickness, which is shown schematically in Fig. 5(a).

Practically, owing to the variation of particle conditions, such as spray particle size, particle velocity, the thickness

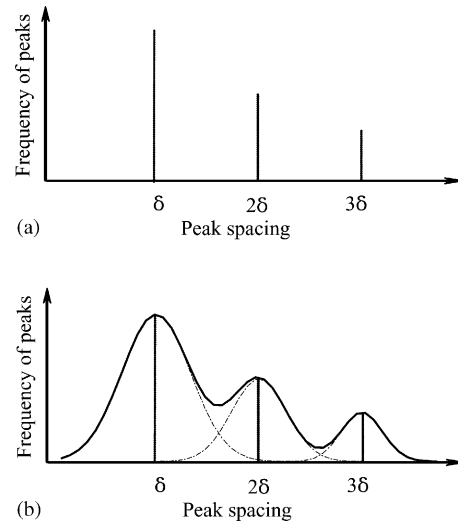


Fig. 5. Schematic of distributions of the peak spacing: (a) for the idealized microstructure model of the lamellae of identical thickness; and (b) for a practical coating with lamellae of the thickness with a Gaussian distribution.

of the lamellae may follow a certain distribution, for example, a Gaussian distribution. The frequency of the peak of the tracer as a function of the peak spacing will present a distribution as shown schematically in Fig. 5(b). Such a distribution results from the superimposing of several individual characteristic peaks with the centers at integer times of the mean lamellae thickness. Therefore, based on the peak processing of the observed peak spacing distribution, the mean lamellae thickness can be obtained by the following equation

$$\delta = \frac{\sum_{j=1}^n A_j T_j}{\sum_{j=1}^n j A_j} \quad (2)$$

where  $A_j$  is the area of the peak centered at  $j$  times of lamellar thickness, and  $T_j$  center of the peak centered at  $j$  times of lamellar thickness. For the idealized microstructure of identical lamellae thickness,  $T_j$  is equal to  $j$  times of lamellar thickness, i.e.,  $j\delta$ .

According to the model shown in Fig. 4, the mean bonding ratio can be calculated by the following equation using the parameters of the characteristic peaks as shown in Fig. 5(b).

$$\alpha = \frac{N_b}{N_t} = \frac{\sum_{j=1}^n (j-1) N_{j\delta}}{\sum_{j=1}^n j N_{j\delta}} = \frac{\sum_{j=1}^n (j-1) A_{j\delta}}{\sum_{j=1}^n j A_{j\delta}} \quad (3)$$

where  $N_b$  is number of the bonded interfaces,  $N_t$  total interface number,  $N_{j\delta}$  number of the interfaces contained in the peak centered at spacing of  $j\delta$ .

Because the maximum bonding ratio between flattened particles revealed by previous studies is about 32% [2,12], and the splat formation behavior for individual molten droplets in thermal spraying is independent [17], the probability for more than three adjacent lamellae bonded together

is less than one percent. Consequently the conditions with more than three adjacent lamellae bonded together can be neglected. Accordingly, it can be considered that the lamella thicker than  $3\delta$  in the model results from partially or unmelted particle. Therefore, Eq. (3) reduces to the following form

$$\alpha = \frac{N_b}{N_t} = \frac{N_{2\delta} + 2N_{3\delta}}{N_{1\delta} + 2N_{2\delta} + 3N_{3\delta}} = \frac{A_2 + 2A_3}{A_1 + 2A_2 + 3A_3} \quad (4)$$

Therefore, through a counting of the tracer peaks obtained by EDX analysis and the analysis of the peak distribution with peak spacing, the mean lamellae thickness, the mean lamellar bonding ratio at the lamellar interfaces, the width of the void at the non-bonded interface can be obtained.

### 3. Processing approach for the tracer peak from the EDX data

#### 3.1. Model for the interaction of electron beam with the tracer in EDX analysis

Based on the model proposed above, it is necessary to establish a suitable method for processing the EDX digital signals to discriminate the individual peaks of the tracer across the lamellar voids. Because the evolution of the signal during the EDX analysis depends on the interaction of the active zone of the electron beam with the tracer filling the lamellar voids, the X-rays intensity measured evolves as the convolution of the beam intensity distribution in the active zone of the electron beam and the volume of the tracer involved. It was indicated that the rate of diffusion of secondary electrons increases as the excitation depth increases up to a layer of 40–50 Å whereas the secondary electrons excited diffuse more widely, in this case the ratio of full width at half-maximum of distribution of secondary electrons to the base was larger than 70% [18]. The intensity distribution in the spot can be considered as a constant. Supposing at the present stage in this study that the excited active zone by the electron beam during the EDX analysis has a circular geometry and the intensity of X-rays from the analyzing element over the active zone is uniform, the intensity of the EDX peak is simply proportional to the overlapped area of the circular active spot with the void filled with the tracer.

#### 3.2. Evolution of individual signal peaks and EDX signal

The interaction of the active zone with the lamellar tracer has been schematically illustrated in Fig. 3. With the movement of the electron beam forward, the active zone gradually enters an area filled with tracer. The characteristic X-rays excited are detected. The intensity of the X-rays increases with the movement of the electron beam and is proportional to the overlapped area of the active zone over tracer.

The intensity reaches a maximum level when the center of the active zone is coincident with the center of the lamellar tracer as shown in Fig. 3. This maximum depends on the relative width of the lamellar tracer to the active zone diameter.

The waveform of the pulse peak can be considered theoretically in the following three cases according to the relative ratio of the diameter of the active zone to the lamellar gap width:

type I:  $\beta_i \leq D/2$ ;

type II:  $D/2 < \beta_i \leq D$ ; and

type III:  $\beta_i > D$ .

The intensity of the signal for an individual pulse peak can be expressed by the following equation based on a calculation of the overlapping areas of the active zone with the lamellar interface gap.

$$I = F_i(D, X_i, x, \beta_i) = k f_i(D, X_i, x, \beta_i) \quad (5)$$

where  $I$  is the intensity of the signal and is a function of  $D, X_i, x, \beta_i, f_i$  representing the overlapped area and  $k$  is a constant related to the intensity distribution over the active zone. The specific forms of above equation corresponding to the above three types are given in the appendix. Those equations are expressed theoretically in five regions. Accordingly, three parameters are needed to describe an individual peak, i.e.,  $D, \beta_i$  and  $X_i$ .

Typical waveforms of  $f_i$  corresponding to three types are shown schematically in Fig. 6. The waveform changes with the ratio of the void width to the diameter of the active zone. In the case of large void corresponding to type III, since the width of the void is larger than the diameter of the active zone, the active zone enters fully into the non-bonded interface in stage III. Consequently, the signal intensity reaches to a saturated maximum. This maximum level will be maintained until the active zone reaches the other side of the non-bonded interface. As a result, there appears a flat segment of a width of  $\beta_i - D$  in the waveform, as shown in Fig. 6(c). As for type I and type II signals, the maximum level of the signal is less than the saturated level and increases with an increase in the width of the void, as shown in Fig. 6(a) and (b).

Unlike the other two parameters  $\beta_i$  and  $X_i$ , whose initialization was determined through processing the signal peak, the initialization of the diameter of the active zone  $D$  was determined before the processing of signal peak. From the type III signal, it could be found that the abscissa of the first inclined part corresponded to  $D$ . Therefore, the initialization of  $D$  could be obtained by processing the signal peak of the EDX line analysis along a relatively large pore. Then through the data processing shown in Section 3.3, the best fit of  $D$  could be obtained. If  $D$  is changed, the waveform of the pulse peak for the particular lamella is changed too. This is because the type of waveform depends on the ratio of  $D$  to  $\beta_i$ . However, such change do not alter the fitting results of other parameters.



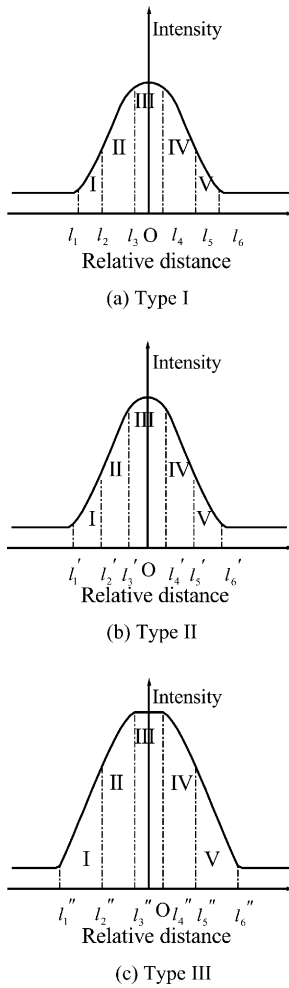


Fig. 6. Schematic of typical waveforms of three types of EDX signals divided by the ratio of the active zone diameter to the width of interface voids: (a) type I,  $\beta_i \leq D/2$ ; (b) type II,  $D/2 < \beta_i \leq D$ ; (c) type III,  $\beta_i > D$ .

Supposing that the intensity of the detected signal is a result of  $n$  independent peaks expressed by  $kf_i(D, X_i, x, \beta_i)$  ( $i = 1, 2, 3, \dots, n$ ), the total intensity of the tracer as a function of abscissa along the EDX analyzing line ( $x$ ) can be expressed as

$$I = F(x) = \sum_{i=1}^n F_i(D, X_i, x, \beta_i) = \sum_{i=1}^n kf_i(D, X_i, x, \beta_i) \quad (6)$$

Practically, the distribution of the intensity of the excited characteristic X-rays in the active zone during EDX analysis is not a constant. Therefore, the above equation should be modified according to a distribution function of the excited X-rays intensity in the active zone. In this study, it was supposed that the integral distribution function of the excited X-rays followed a Gaussian distribution. This distribution function can be used to modify the Eq. (6). Accordingly, the intensity

of the tracer along a line becomes

$$F(x) = \sum_{i=1}^n F_i(D, X_i, x, \beta_i) = \sum_{i=1}^n \left( \frac{A_G}{W_G \sqrt{\pi/2}} e^{(-2(x-X_i)^2)/W_G^2} \right) f_i(D, X_i, x, \beta_i) + F_0 \quad (7)$$

where  $W_G$  is 0.849 the half-width of the Gaussian distribution and  $A_G$  is the area of the Gaussian distribution,  $F_0$  is the baseline offset.

Based on the data fitting to the above equation, individual peaks in EDX analysis data can be separated and subsequently the functions  $f_i$  of individual peaks can be obtained. As a result, both position and width for individual interlamellar gaps can be calculated.

### 3.3. Processing procedure of EDX data of the tracer for peak parameters

To separate individual peaks from EDX line analysis data and obtain peak parameters for individual peaks, a data processing method was established. Data processing procedures included reduction of noise, identification of individual peak, separation of overlapped peaks, and calculation of individual peak parameters. The noise reduction from signal was performed by data smoothing. The identification of the individual peak maximum position was carried out through two-order differential of the detected EDX line analysis data. The further sorting out of the peak was based on a  $3\sigma$  criteria with which the peak of maximum intensity less than  $3\sigma$  from average baseline level was removed as noise. With certain initial parameters for individual peaks, the fitting of data with Eq. (7) was carried out through least-squares estimation proposed in the literature [19]. Because every peak corresponded to a non-bonded interface void, through the above data processing procedures, peak numbers over the analysis line and the parameters of individual peaks could be calculated. Those data included abscissa of the center of the peak corresponding to the location of the non-bonded interface and the width of non-bonded interfaces. Accordingly, the mean lamellae thickness, the bonding ratio and average width of non-bonded interface gap could be calculated.

## 4. Experimental results

### 4.1. Materials and experimental procedures

Commercially available alumina powder of particle size from 20 to 40  $\mu\text{m}$  was used in plasma spraying. Mild steel plate of 2 mm in thickness was used as a substrate.  $\text{Al}_2\text{O}_3$  coating was deposited on the grit-blasted substrate surface to a thickness of about 100  $\mu\text{m}$  using a commercial plasma spraying system (GP-80, JIUJIANG, 80 kW). Argon was used as a primary plasma operating gas and hydrogen was

used as an auxiliary gas. During spraying the pressures of both argon and hydrogen were fixed at 0.7 and 0.4 MPa, respectively. The flow of the primary gas was fixed at 47.1 l/min, and the auxiliary gas 10.5 l/min. Nitrogen was used as powder feed gas, and the powder feed rate was about 8 g/min. During spraying, the gun, which was held horizontally, was set to traverse back and forth across sample surface with a step of 3 mm at a torch–substrate distance of 110 mm.

The sprayed coating was immersed into a saturated chromic acid solution for 10 min and then heat-treated in a furnace at a temperature of 550 °C to make the chromium acid decompose completely to deposit  $\text{Cr}_2\text{O}_3$  into the voids in the coating. This process was repeated 13 times to assure sufficient deposition of  $\text{Cr}_2\text{O}_3$  into the voids in the coating. After infiltration, the specimen was prepared for the examination of cross-sectional microstructure by SEM. The EDX line analysis perpendicular to the lamellae was carried out to obtain line distribution of Cr element resulting from the infiltrated  $\text{Cr}_2\text{O}_3$  using EDX analyzer line by line. The EDX line analysis was carried out using EDX analyzer (Link ISIS, Oxford) attached to SEM (JSM-5800 JEOL). The voltage and current of the beam were 20 V and 70  $\mu\text{A}$ , respectively. The working distance was 12 mm. The EDX signals were recorded in digital form for the processing to evolve the structure parameters.

#### 4.2. Processing of EDX signal

Fig. 2(b) shows one typical original digital signal of chromium distribution obtained by EDX line analysis. The spaces occupied by the infiltrated  $\text{Cr}_2\text{O}_3$  that were indicated by EDX Cr peaks corresponded to the gaps in the as-sprayed coating. Such data were processed through smoothing, peak-picking, peak-fitting techniques to obtain the individual peak in a separate form. Fig. 7(a) shows the obtained individual peaks in a separate wave form and Fig. 7(b) illustrates the line distribution data with all individual peaks superimposed on. With the parameters of individual peaks as shown in Fig. 7(a), the structural parameters can be calculated using the model proposed earlier.

#### 4.3. Mean lamellae thickness and mean bonding ratio

Fig. 8 shows the observed distribution of the peak spacing of the  $\text{Al}_2\text{O}_3$  coating using different cumulative lengths of measurement obtained by a number of scanning lines which traversed the cross-section of the coatings. It was found that when the total length of scanning lines was short, e.g. 500  $\mu\text{m}$ , as shown in Fig. 8(a), it was difficult to identify the distribution of the peak spacing for multiple peaks. With the increase in the total length of scanning lines, e.g. up to 1260  $\mu\text{m}$ , as shown in Fig. 8(b), the individual peaks became evident. As the distribution of the peak spacing was calculated from the cumulative scanning line length of 2680  $\mu\text{m}$ , as shown in Fig. 8(c), it was clear that the peak spacing exhibited a multimodal distribution as expected theoretically (see Fig. 5(b)).

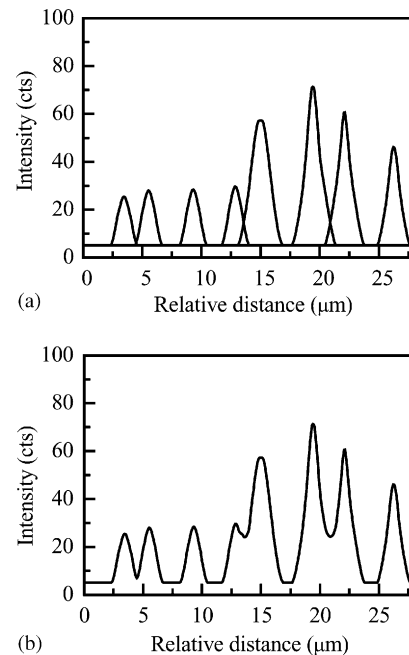


Fig. 7. (a) Illustrations of individual peaks separated from the data shown in Fig. 2(b); and (b) reconstruction of the peaks.

Accordingly, the mean lamellae thickness and the mean bonding ratio were calculated based on the method proposed in Section 2.3. To clarify the cumulative length of scanning lines necessary for a statistical analysis, its effect on the mean lamellae thickness and mean bonding ratio were investigated. The results as the variations in the mean lamellae thickness and the mean bonding ratio with the cumulative length of scanning lines are shown in Figs. 9 and 10, respectively. It was clear that the mean lamellae thickness and the mean bonding ratio varied largely when the length of scanning lines was short, and tended to approach to a certain value with a further increase in the analyzing line length. It was found that when the length of scanning lines exceeded 1260  $\mu\text{m}$ , the variations in the mean lamellae thickness and the mean bonding ratio all dropped to less than  $\pm 10\%$ , and the mean lamellae thickness and the bonding ratio became independent of the length of scanning lines. Therefore, scanning lines, at least 1260  $\mu\text{m}$  long, are necessary to obtain statistically reliable mean lamellae thickness and the mean bonding ratio for plasma-sprayed  $\text{Al}_2\text{O}_3$  coatings.

Using the data obtained from the scanning line 2680  $\mu\text{m}$  long, the three peaks in the spacing distribution yielded the centers of 1.0, 2.4 and 4.2  $\mu\text{m}$ , respectively. The characteristic parameters of those three peaks fitted by the Gaussian distribution are shown in Table 1. The mean bonding ratio of 32% and the mean lamellae thickness of 1.2  $\mu\text{m}$  were obtained for the  $\text{Al}_2\text{O}_3$  coatings used in the present study.

Previous results [2,11,12] obtained using the copper plating technique revealed that the mean bonding ratio of plasma-sprayed  $\text{Al}_2\text{O}_3$  coating changed with the change of spray distance from 80 to 150 mm. The coating sprayed at spray

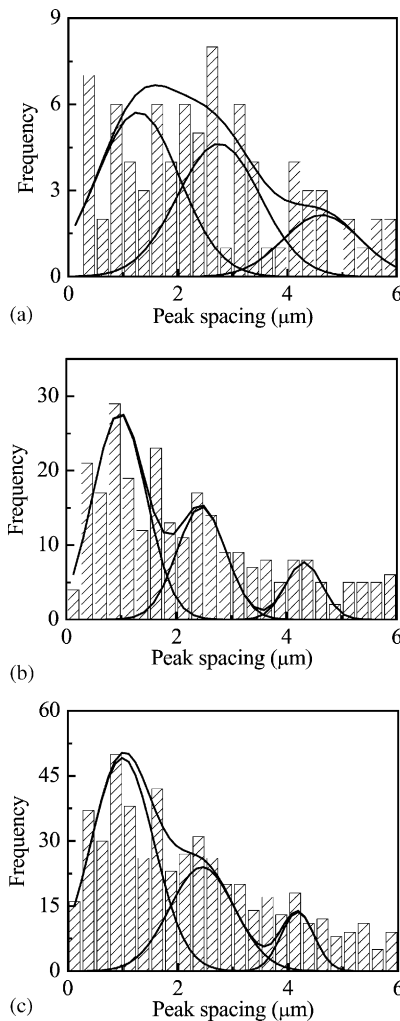


Fig. 8. Effect of the cumulative analysis length on the distribution of the peak spacing of Al<sub>2</sub>O<sub>3</sub> coating: (a) 500 μm; (b) 1260 μm; and (c) 2680 μm.

distance up to 100 mm exhibited a mean bonding ratio of about 32%. When the spray distance was increased further to 150 mm, the mean bonding ratio decreased sharply to 18.6%. The maximum mean bond ratio obtained was about 32%. Those results correlated well with the properties of plasma-sprayed coatings [6,20].

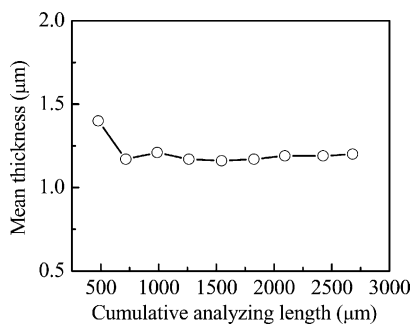


Fig. 9. Effect of the cumulative analysis length on the mean thickness of lamella.

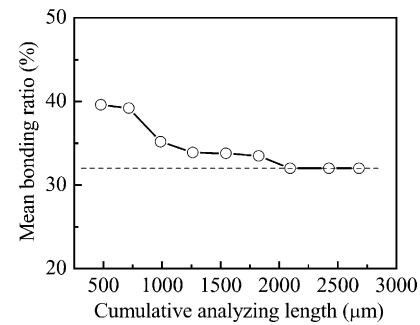


Fig. 10. Effect of the cumulative analysis length on the mean bonding ratio.

Table 1

Characteristic parameters of the peak spacing distribution fitted by the Gaussian distribution

Peak number	Area (μm <sup>2</sup> )	Center (μm)	Width (μm)	Height (μm)
1	70.2	1.0	1.1	49.2
2	35.4	2.4	1.4	24.0
3	10.2	4.2	1.1	13.6

#### 4.4. Width distribution of lamellar interface voids

The distribution of the width of lamellar interface voids is shown in Fig. 11. It was found that the width of the non-bonded interfaces exhibited a bimodal distribution. One peak appeared at 0.09 μm and the other at 1.11 μm. From Fig. 2(a), it can be found that because the EDX analyzing line in this study was perpendicular to the splat plane, it might pass voids of the microcrack type in the direction of cracking. Consequently, the large width was interpreted as a conventional coarse pore, which corresponded to the conventional coarse pore with the same dimensions of lamellar thickness and microcrack type pore. The lamellar interface voids with a width of 0.09 μm corresponded to the interlamellar voids. Therefore, the distribution of the non-bonded interface gaps in the bimodal agrees well with the bimodal distribution of the pores in the coating [7].

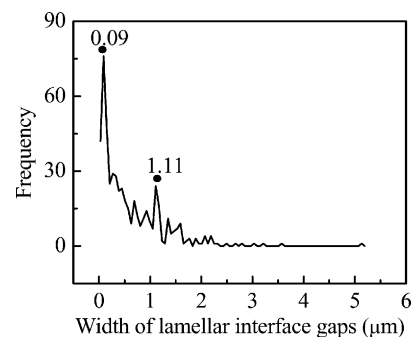


Fig. 11. Distribution of the width of the non-bonded interface gaps of plasma-sprayed Al<sub>2</sub>O<sub>3</sub> coating.



## 5. Conclusions

The visualization of the distribution of the voids in a thermally sprayed coating was realized by analyzing the distribution of a tracer filled the voids of the as-sprayed coating. A method for the quantitative characterization of the microstructure of plasma-sprayed coating using structural parameters with EDX line analyzing data of the tracer was proposed on the basis of theoretical analysis of an idealized microstructural model. The microstructural parameters included the mean thickness of the flattened particles, the mean bonding ratio between the flattened particles and the distribution and average width of the non-bonded interface gaps. The experimental correlation was carried out using plasma-sprayed  $\text{Al}_2\text{O}_3$  coating infiltrated with  $\text{Cr}_2\text{O}_3$  in the voids of the as-sprayed coating. The existence of the non-bonded interface areas was visually revealed by EDX line analysis data of the Cr distribution along lines perpendicular to the lamellae resulting from the infiltrated  $\text{Cr}_2\text{O}_3$  tracer. A data processing method for the EDX line data was established to separate individual peak and calculate peak parameters. The calculation of the mean lamellar bonding ratio, the mean lamellae thickness and the non-bonded interface gaps distribution showed that a certain number of analyzing lines corresponding to a certain cumulative analyzing length were necessary to statistically calculate the mean values of the structural parameters.

A mean bonding ratio of 32% and a mean thickness of the flattened particles of 1.2  $\mu\text{m}$  obtained for plasma-sprayed  $\text{Al}_2\text{O}_3$  coating were reasonably consistent with data reported previously. The width of the non-bonded interface gap exhibited a reasonable bimodal distribution. Therefore, the present method can be practically applied to quantitatively evaluate the microstructure of plasma-sprayed coatings using structural parameters rather than porosity.

## Acknowledgements

The present project was financially supported by the Trans-Century Training Programme Foundation for Talent of the Chinese Education Ministry. Authors would like to express thanks to Mr. Yong He and Miss Hong-Yu Wang for their contributions to the present work.

## Appendix A. The forms of peak functions

### $F_i(D, X_i, l, \beta_i)$

In the case type I,  $F_i(D, X_i, l, \beta_i)$  can be expressed by following functions corresponding to five different regions indicated in Fig. 6:

$$F_i(D, X_i, l, \beta_i) = \begin{cases} k \left[ \left( \frac{D}{2} \right)^2 \arccos \left( \frac{-l - (\beta_i/2)}{D/2} \right) - \left( -l - \frac{\beta_i}{2} \right) \sqrt{\left( \frac{D}{2} \right)^2 - \left( -l - \frac{\beta_i}{2} \right)^2} \right] & l_1 < l \leq l_2 \\ k \left[ \left( \frac{D}{2} \right)^2 \arccos \left( \frac{-l - (\beta_i/2)}{D/2} \right) - \left( -l - \frac{\beta_i}{2} \right) \sqrt{\left( \frac{D}{2} \right)^2 - \left( -l - \frac{\beta_i}{2} \right)^2} - \left( \frac{D}{2} \right)^2 \arccos \left( \frac{(\beta_i/2) - l}{D/2} \right) + \left( \frac{\beta_i}{2} - l \right) \sqrt{\left( \frac{D}{2} \right)^2 - \left( \frac{\beta_i}{2} - l \right)^2} \right] & l_2 < l \leq l_3 \\ k \left[ \pi \left( \frac{D}{2} \right)^2 - \left( \frac{D}{2} \right)^2 \arccos \left( \frac{(\beta_i/2) + l}{D/2} \right) - \left( \frac{D}{2} \right)^2 \arccos \left( \frac{(\beta_i/2) - l}{D/2} \right) + \left( \frac{\beta_i}{2} + l \right) \sqrt{\left( \frac{D}{2} \right)^2 - \left( \frac{\beta_i}{2} + l \right)^2} + \left( \frac{\beta_i}{2} - l \right) \sqrt{\left( \frac{D}{2} \right)^2 - \left( \frac{\beta_i}{2} - l \right)^2} \right] & l_3 < l \leq l_4 \\ k \left[ \left( \frac{D}{2} \right)^2 \arccos \left( \frac{l - (\beta_i/2)}{D/2} \right) - \left( l - \frac{\beta_i}{2} \right) \sqrt{\left( \frac{D}{2} \right)^2 - \left( l - \frac{\beta_i}{2} \right)^2} - \left( \frac{D}{2} \right)^2 \arccos \left( \frac{(\beta_i/2) + l}{D/2} \right) + \left( \frac{\beta_i}{2} + l \right) \sqrt{\left( \frac{D}{2} \right)^2 - \left( \frac{\beta_i}{2} + l \right)^2} \right] & l_4 < l \leq l_5 \\ k \left[ \left( \frac{D}{2} \right)^2 \arccos \left( \frac{l - (\beta_i/2)}{D/2} \right) - \left( l - \frac{\beta_i}{2} \right) \sqrt{\left( \frac{D}{2} \right)^2 - \left( l - \frac{\beta_i}{2} \right)^2} \right] & l_5 < l \leq l_6 \end{cases}$$

In the case type II, the form of the function  $F_i(D, X_i, l, \beta_i)$  becomes:

$$F_i(D, X_i, l, \beta_i) = \begin{cases} k \left[ \left( \frac{D}{2} \right)^2 \arccos \left( \frac{-l - (\beta_i/2)}{D/2} \right) - \left( -l - \frac{\beta_i}{2} \right) \sqrt{\left( \frac{D}{2} \right)^2 - \left( -l - \frac{\beta_i}{2} \right)^2} \right] & l'_1 < l \leq l'_2 \\ k \left[ - \left( \frac{D}{2} \right)^2 \arccos \left( \frac{(\beta_i/2) + l}{D/2} \right) + \left( \frac{\beta_i}{2} + l \right) \sqrt{\left( \frac{D}{2} \right)^2 - \left( \frac{\beta_i}{2} + l \right)^2} + \pi \left( \frac{D}{2} \right)^2 \right] & l'_2 < l \leq l'_3 \\ k \left[ \left( \frac{\beta_i}{2} + l \right) \sqrt{\left( \frac{D}{2} \right)^2 - \left( \frac{\beta_i}{2} + l \right)^2} - \left( \frac{D}{2} \right)^2 \arccos \left( \frac{(\beta_i/2) + l}{D/2} \right) + \sqrt{\left( \frac{D}{2} \right)^2 - \left( \frac{\beta_i}{2} - l \right)^2} \left( \frac{\beta_i}{2} - l \right) - \left( \frac{D}{2} \right)^2 \arccos \left( \frac{(\beta_i/2) - l}{D/2} \right) + \pi \left( \frac{D}{2} \right)^2 \right] & l'_3 < l \leq l'_4 \\ k \left[ - \left( \frac{D}{2} \right)^2 \arccos \left( \frac{(\beta_i/2) - l}{D/2} \right) + \left( \frac{\beta_i}{2} - l \right) \sqrt{\left( \frac{D}{2} \right)^2 - \left( \frac{\beta_i}{2} - l \right)^2} + \pi \left( \frac{D}{2} \right)^2 \right] & l'_4 < l \leq l'_5 \\ k \left[ \left( \frac{D}{2} \right)^2 \arccos \left( \frac{l - (\beta_i/2)}{D/2} \right) - \left( l - \frac{\beta_i}{2} \right) \sqrt{\left( \frac{D}{2} \right)^2 - \left( l - \frac{\beta_i}{2} \right)^2} \right] & l'_5 < l \leq l'_6 \end{cases}$$

In the case type III, the function  $F_i(D, X_i, l, \beta_i)$  takes following forms:

$$F_i(D, X_i, l, \beta_i) = \begin{cases} k \left[ \left(\frac{D}{2}\right)^2 \arccos\left(\frac{-l-(\beta_i/2)}{D/2}\right) - \left(-l - \frac{\beta_i}{2}\right) \sqrt{\left(\frac{D}{2}\right)^2 - \left(-l - \frac{\beta_i}{2}\right)^2} \right] & l_1' < l \leq l_2'' \\ k \left[ -\left(\frac{D}{2}\right)^2 \arccos\left(\frac{(\beta_i/2)+l}{D/2}\right) + \left(\frac{\beta_i}{2} + l\right) \sqrt{\left(\frac{D}{2}\right)^2 - \left(\frac{\beta_i}{2} + l\right)^2} + \pi\left(\frac{D}{2}\right)^2 \right] & l_2'' < l \leq l_3' \\ k\pi\left(\frac{D}{2}\right)^2 & l_3'' < l \leq l_4'' \\ k \left[ -\left(\frac{D}{2}\right)^2 \arccos\left(\frac{(\beta_i/2)-l}{D/2}\right) + \left(\frac{\beta_i}{2} - l\right) \sqrt{\left(\frac{D}{2}\right)^2 - \left(\frac{\beta_i}{2} - l\right)^2} + \pi\left(\frac{D}{2}\right)^2 \right] & l_4' < l \leq l_5'' \\ k \left[ \left(\frac{D}{2}\right)^2 \arccos\left(\frac{l-(\beta_i/2)}{D/2}\right) - \left(l - \frac{\beta_i}{2}\right) \sqrt{\left(\frac{D}{2}\right)^2 - \left(l - \frac{\beta_i}{2}\right)^2} \right] & l_5'' < l \leq l_6' \end{cases}$$

where,  $l_1 = l_1' = l_1'' = -\frac{\beta_i}{2} - \frac{D}{2}$ ;  $l_2 = l_2' = l_2'' = \frac{\beta_i}{2} - \frac{D}{2}$ ;  $l_3 = l_3' = l_3'' = -\frac{\beta_i}{2}$ ;  $l_4 = l_4' = l_4'' = \frac{\beta_i}{2}$ ;  $l_5 = l_5' = l_5'' = \frac{D}{2} - \frac{\beta_i}{2}$ ; and  $l_6 = l_6' = l_6'' = \frac{\beta_i}{2} + \frac{D}{2}$

## References

- [1] C.-J. Li, A. Ohmori, R. McPherson, J. Mater. Sci. 32 (1997) 997–1004.
- [2] A. Ohmori, C.-J. Li, Thin Solid Films 201 (1991) 241–252.
- [3] S. Kuroda, T.W. Clyne, Thin Solid Films 200 (1991) 49–66.
- [4] M. Vardelle, J.-L. Besson, Ceram. Int. 7 (1981) 48–54.
- [5] S. Kuroda, in: P. Vincenzini (Ed.), Advances in Inorganic Films and Coatings, 1995, pp. 373–380.
- [6] C.-J. Li, A. Ohmori, J. Therm. Spray Technol. 11 (2002) 365–374.
- [7] R. McPherson, B.V. Shafer, Thin Solid Films 97 (1982) 201–204.
- [8] J. Ilavsky, G.G. Long, A.J. Allen, L. Leblanc, M. Prystay, C. Moreau, J. Therm. Spray Technol. 8 (1999) 414–420.
- [9] J. Ilavsky, J. Pisacka, P. Chraska, N. Margandant, et al., in: C.C. Berndt (Ed.), Thermal Spray: Surface Engineering via Applied Research, Quebec: ASM International, Materials Park, OH, 2000, pp. 449–454.
- [10] M.F. Smith, D.T. McGuffin, J.A. Henfling, W.B. Lenling, in: T.F. Bernecki (Ed.), Thermal Spray Coating, Properties, Processes and Applications, Pittsburgh: ASM International, Materials Park, OH, 1991, pp. 97–104.
- [11] Y. Arata, A. Ohmori, C.-J. Li, in: High Temperature Society of Japan (Ed.), Proceedings of International Symposium on Advanced Thermal Spraying Technology and Allied Coatings, Osaka: Japan High Temperature Society, Osaka, Japan, 1988, pp. 205–210.
- [12] A. Ohmori, C.-J. Li, Y. Arata, Trans. Jpn. Weld. Res. Inst. 19 (1990) 259–270.
- [13] R. McPherson, P. Cheang, in: I.A. Bucklow (Ed.), Proceedings of the 12th International Thermal Spray Conference, London, UK, 1989, pp. 17–1–10.
- [14] S. Boire-Lavigne, C. Moreau, R.G. Saint-Jacques, J. Therm. Spray Technol. 4 (1995) 261–267.
- [15] C. Takahashi, T. Senda, J. Jpn. Therm. Spray. Soc. 30 (1993) 31–41.
- [16] S. Kuroda, T. Dendo, J. Kitahara, J. Therm. Spray Technol. 4 (1995) 75–84.
- [17] J.M. Houben, G.G. van Liempd, Proceedings of the 10th International Thermal Spraying Conference, DVS, Germany Welding Society, Germany, 1983, pp. 66–71.
- [18] T. Koshikawa, R. Shimizu, J. Phys. D 7 (1974) 1303–1315.
- [19] D.W. Marquardt, J. Soc. Ind. Appl. Math. 11 (1963) 431–441.
- [20] R. McPherson, Thin Solid Films 112 (1984) 89–95.